Nano Energy 32 (2017) 454–462

Contents lists available at ScienceDirect

Nano Energy

journal homepage: www.elsevier.com/locate/nanoen

Epitaxial growth of vertically stacked p-MoS_2/n-MoS_2 heterostructures by chemical vapor deposition for light emitting devices

Revannath Dnyandeo Nikam[a,b,c], Poonam Ashok Sonawane[d,e,f], Raman Sankar[g,h], Yit-Tsong Chen[a,b,*]

[a] Department of Chemistry, National Taiwan University, Taipei 106, Taiwan
[b] Institute of Atomic and Molecular Sciences, Academia Sinica, Taipei 106, Taiwan
[c] Nanoscience and Technology Program, Taiwan International Graduate Program, Academia Sinica, Taipei 115, Taiwan
[d] Institute of Chemistry, Academia Sinica, Taipei 115, Taiwan
[e] Department of Applied Chemistry, National Chiao-Tung University, Hsinchu 300, Taiwan
[f] Sustainable Chemical Science and Technology Program, Taiwan International Graduate Program, Academia Sinica, Taipei 115, Taiwan
[g] Center for Condensed Matter Sciences, National Taiwan University, Taipei 10617, Taiwan
[h] Institute of Physics, Academia Sinica, Taipei 10617, Taiwan

ARTICLE INFO

Keywords:
Two-dimensional material
Transition-metal dichalcogenides (TMDC)
Vertical heterostructures
CVD growth of p-MoS_2/n-MoS_2
White light emitting diode (WLED)

ABSTRACT

Despite the dramatic advances of two-dimensional vertical heterostructure, the controlled growth and potential applications in light emitting devices of these heterostructures have not yet been well established. Here, we report, for the first time, the epitaxial growth of two-dimensional p-MoS_2/n-MoS_2 vertical heterostructures by a chemical vapor deposition (CVD) method, where the n-MoS_2 was synthesized first, followed by an epitaxial growth of p-MoS_2 on top of the n-MoS_2 via a control of the growth temperature. Atomic-resolution scanning transmission electron microscopy (STEM) imaging reveals that the vertically stacked bilayer of the hexagram-shaped p-MoS_2/n-MoS_2 preferred the 2H stacking phase during the growth. The structural and optical features of the as-grown p-MoS_2/n-MoS_2 heterostructure were examined by Raman and photoluminescence (PL) spectroscopy. This novel hybrid heterostructure was demonstrated to be an excellent building block for a highly efficient white light emitting diode (WLED). In addition, we transferred the p-MoS_2/n-MoS_2 on top of a p-GaN bilayer to fabricate a tetra-layered (4-L) n-MoS_2/p-MoS_2/p-GaN heterostructure, which could emit electroluminescence (EL) in forward bias. The EL spectra comprise three emission peaks centered at 481 nm (from p-GaN), 525 nm (from p-MoS_2), and 642 nm (from n-MoS_2), with a dominant emission peak located at 642 nm. The WLED device composed of the n-MoS_2/p-MoS_2/p-GaN heterostructure showed a luminance of 30,548 cd/m^2, luminescence efficiency of 29% and the luminous efficacy of 294 lm/W at a bias voltage of 4 V. This work demonstrates that white light emission can be generated from vertically stacked few-layered 2D materials-based heterostructures, which also hold great potential for constructing color-tunable light emitters for low-cost display, lighting, and optical communication.

1. Introduction

Two-dimensional (2D) layered transition metal dichalcogenides (TMDC), discovered after the discovery of graphene, are considered as analogs of graphene [1,2]. Compared to lateral heterojunctions, advances in 2D TMDC layered materials have resulted in a variety of vertically stacked heterostructures constructed with different TMDC combinations [3,4]. TMDCs are regarded as excellent materials for white light emitting diodes (WLEDs) because there is a wide choice of TMDC candidates that offer relatively easy combined stacking. Moreover, many monolayered (1-L) TMDCs are direct band-gap semiconductors, which is promising for developing atomically thin LED devices [5,6]. The recent employment of 2D TMDCs has reinvigorated the fields of nanoscale electronics and optoelectronics due to the unique optical and electrical properties of TMDCs at atomically thin layers [6]. The 1-L MoS_2 shows strong photoluminescence (PL) with a direct band transition at 1.8 eV. Among TMDCs, MoS_2 and its polymorphs could be the most useful constituent materials for photonic devices, e.g., LEDs. MoS_2 can be doped to exhibit either a p-type or n-type nature depending on the oxygen and sulfur contents within the layered structure; n-MoS_2 and p-MoS_2 possess distinct optical and electrical properties [7,8].

* Corresponding author.
E-mail address: ytcchem@ntu.edu.tw (Y.-T. Chen).

http://dx.doi.org/10.1016/j.nanoen.2017.01.006
Received 13 September 2016; Received in revised form 28 December 2016; Accepted 4 January 2017
Available online 05 January 2017

Recently, numerous studies have focused on WLEDs because of their major advantages of high brightness for low-power consumption and long lifetimes for high-performance operation [9–13]. Due to these advantages, WLEDs have great potential for lighting and display applications. To date, significant progress has been made in the development of WLEDs, where the current technological strategies are based on two main tactics. The first design relies on a phosphor-based down-conversion design to transform blue light into green and red light [14–18]. Commercially available phosphor-based WLEDs are mainly constructed of a blue light-emitting InGaN/GaN chip in which the color conversion layer is composed of rare-earth phosphors [19,20]. Upon absorption of a certain fraction of blue light, the phosphor down-converts the absorbed blue light and re-emits across the visible spectral range. However, the fabrication of phosphor-based WLEDs demands rather complicated conditions, such as a high growth temperature, a specially designed electronic configuration, and costly rare-earth phosphors, making these products expensive. The second design is based on organic light emitting diodes (OLEDs) [21–24], which have made the production of large-scale white light devices possible, despite necessitating the multilayered OLED structures for high-performance white light applications. Due to these limitations, the production of white light devices by the present LED technologies is still a challenging task. Therefore, searching for alternative materials as better candidates to improve the performance of WLEDs is highly required in developing an advanced WLED technology.

Until now, the use of MoS_2 and other TMDCs in reported LED devices has been limited to single TMDCs or the lateral heterostructures formed by MoS_2 and other TMDCs [25,26]. Recently, CVD methods have been developed to grow lateral heterostructures of different TMDCs [27–30]. However, the main drawback associated with lateral heterostructures is the alloy formed at the boundary regions, which limits their applications in LED technology. In contrast, the vertical heterostructures of 2D TMDCs [31] present many advantages over lateral heterostructures in LED technology, such as reduced contact resistance, higher current densities for brighter LEDs, and luminescence from the whole device area [6,32,33]. In this context, we report on the vertical heterostructure of n-MoS_2/p-MoS_2/p-GaN, which can emit white light and has many advantages over traditional LEDs, such as an ability to create atomically thin devices with simple device structures, a low operating potential, and high luminescence.

2. Experimental section

2.1. Synthesis of vertically stacked p-MoS_2/n-MoS_2 heterostructures

Molybdenum oxide (MoO_3, 99%) and sulfur powder (S, 99%) were purchased from Sigma Aldrich. The vertical heterostructures of p-MoS_2/n-MoS_2 were synthesized in a two-step CVD process. In the first step, triangular 1-L n-MoS_2 single crystals were formed on SiO_2/Si substrates (represented as n-MoS_2/SiO_2/Si). In the second step, the as-grown n-MoS_2/SiO_2/Si was used as the growth substrate to synthesize p-MoS_2. In the reaction, 10 mg of pure MoO_3 was placed in an alumina crucible at a location near the maximum temperature of 600 °C in the furnace. At the gas inlet of the reaction tube, a container with 0.5 g of sulfur power was placed at 170 °C. Several n-MoS_2/SiO_2/Si substrates, on which p-MoS_2 was designated to grow at 530 °C to form vertically stacked p-MoS_2/n-MoS_2 heterostructures, were placed close to each other in the growth region. Before the crystal growth, the CVD system was vented with Ar at 200 sccm for 15 min. The center of the furnace was gradually heated from room temperature to 600 °C in 24 min at the rate of ~25 °C/min. As the temperature approached 500 °C, the sulfur started to evaporate slowly. During the synthetic reaction, the CVD system was maintained at 100 Torr with an Ar flow of 40 sccm. After a 10–15 min reaction, the furnace was cooled down to room temperature under ambient conditions.

2.2. Characterization of vertically stacked p-MoS_2/n-MoS_2 heterostructures

The surface morphologies of the as-grown products were examined using a scanning electron microscope (SEM) (FEI, Nova 200) equipped with an energy-dispersive X-ray (EDX) spectrometer. The microstructural analyses were conducted in a high-resolution transmission electron microscope (HRTEM) (Tecnai F30) equipped with X-ray energy dispersive spectroscopy (EDS). To gain insight into the electronic structures of the bilayer p-MoS_2/n-MoS_2 heterojunction, ultraviolet photon spectroscopy (UPS) measurements were conducted using an ESCALAB 250Xi UPS system (Thermo Scientific). The work function of MoS_2 was calculated from the difference between the cutoff of the highest binding energy and the photon energy of the exciting radiation (Supporting information Section S1 and Fig. S1). Additionally, the edge of valence band (VB) can be calculated from the onset of the lowest binding energy. Chemical configurations were determined by X-ray photoelectron spectroscopy (XPS, Phi V5000), which was performed on the samples with a Mg Kα X-ray source. The energy calibrations were made against the C 1s peak to eliminate the charging current of the sample during analysis. Room temperature PL measurements were obtained using a 488 nm solid-state laser as the excitation source. The 488 nm laser was focused on the sample surface with a spot size of ~1 µm through an objective lens (×100, N.A. =0.9). The PL signals were then collected by the same objective lens, analyzed by a 75 cm monochromator, and finally detected with a liquid-nitrogen cooled charge-coupled device (CCD) camera. Micro-Raman spectra were collected in a confocal Raman spectrometer (NTEGRA Spectra, NT-MDT) with a 488 nm excitation laser, which was focused to a spot size of~0.5 µm on the sample surface; the spectral resolution of the system is ~1 cm^{-1} obtained via a grating of 1800 grooves/mm.

2.3. Fabrication and characterization of LED devices

The LED devices were fabricated by transferring the already-synthesized p-MoS_2/n-MoS_2 heterostructure on to the as-grown p-GaN/sapphire with an etching-free transfer method. After the transfer, a pair of Au (50 nm)/Cr (2 nm) electrodes was deposited in a thermal evaporator. The electroluminescence (EL) spectra were recorded in forward bias with a fluorescence spectrophotometer (F-4500, Hitachi) along with an optics integrating sphere and the LED measurement starter packages. The electrical and optical characteristics of the devices were measured using a Keithley 2400 source meter and a Newport 1835 C optical meter.

3. Results and discussion

The schematic illustration for the formation of vertical heterostructures of p-MoS_2/n-MoS_2 is shown in Fig. 1. The atomically stacked thin layers of p-MoS_2/n-MoS_2 were synthesized on a SiO_2 (300 nm in thickness)/Si substrate in the two-step chemical vapor deposition (CVD) reaction. Fig. 1**(A)** illustrates the experimental setup of the CVD growth in high yield of vertical heterostructures of p-MoS_2/n-MoS_2 with a bilayer triangular feature. The detailed mechanism for the epitaxial growth of vertical heterostructures of hexagram-shaped p-MoS_2/n-MoS_2 is schematically illustrated in Fig. 1**(B)**. In this epitaxial growth, monolayer single-crystal n-MoS_2 was first formed at a higher growth temperature, followed by the formation of monolayer single-crystal p-MoS_2 on the basal plane of the existing n-MoS_2 crystal at a lower growth temperature. In the first step, the n-type 1-L MoS_2 triangular domains were synthesized at 700 °C on a SiO_2/Si substrate by the complete reduction and sulfuration of a molybdenum trioxide (MoO_3) precursor, as shown in **Eq.** (1):

$$2MoO_3+7\,S\rightarrow 2MoS_2+3SO_2 \tag{1}$$

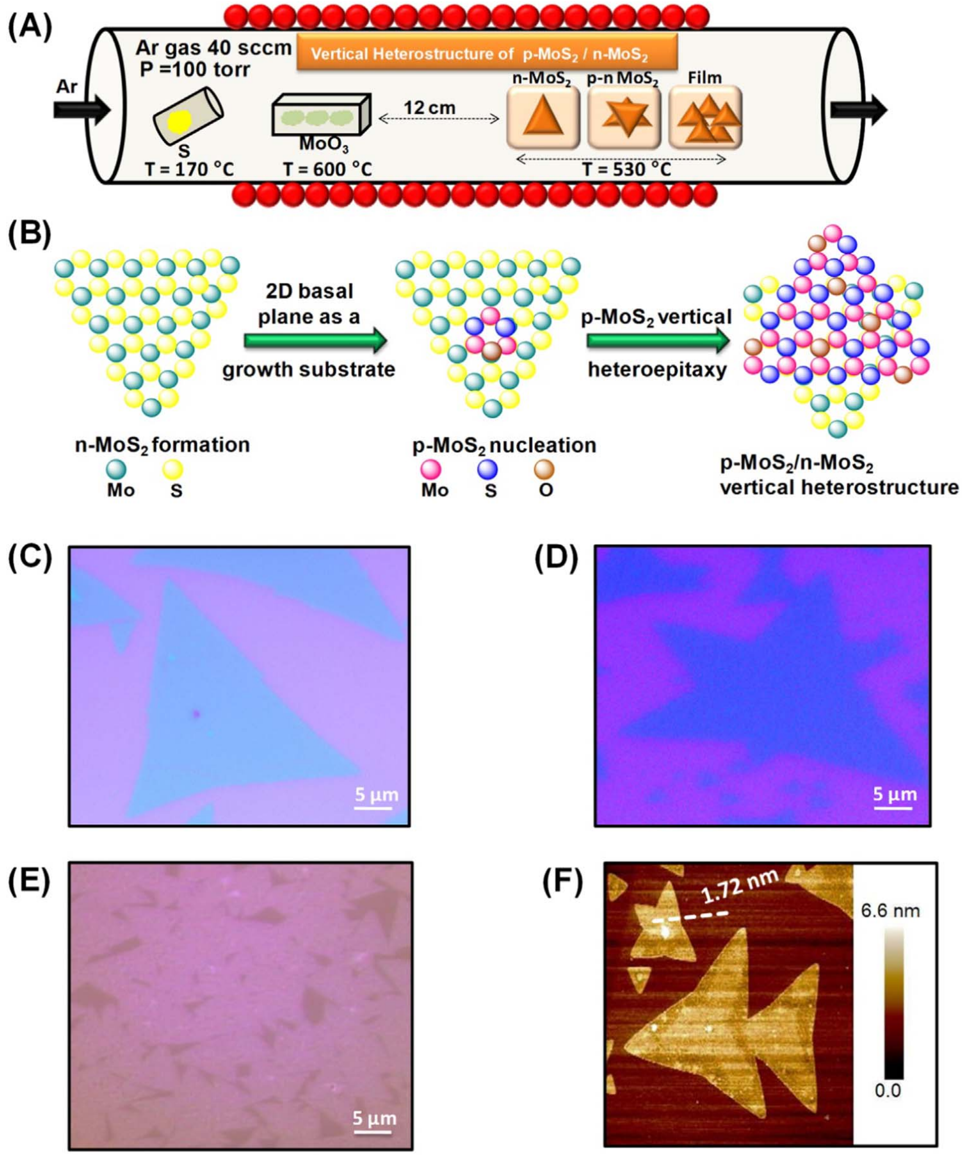

Fig. 1. Synthesis of p-MoS_2/n-MoS_2 heterostructures. (A) Illustration of the CVD growth of the vertically stacked p-MoS_2/n-MoS_2 heterostructure. (B) Schematic representation of the epitaxial growth process of the vertical heterostructures of p-MoS_2/n-MoS_2. (C–E) OM images of (C) monolayer single-crystal n-MoS_2 triangular islands, (D) bilayer single-crystal vertical heterostructures of p-MoS_2/n-MoS_2, and (E) a continuous MoS_2 film on a SiO_2/Si substrate. (F) AFM topograph of the vertically stacked p-MoS_2/n-MoS_2 bilayer on a SiO_2/Si substrate with the bilayer height of 1.72 nm.

The triangular morphology of the 1-L n-MoS_2 single crystal was examined by optical microscopy (OM). Fig. 1**(C)** shows an OM image of isolated triangular islands of the n-MoS_2 on a SiO_2/Si substrate (represented as n-MoS_2/SiO_2/Si). The edge lengths of the triangular islands varied from several micrometers to tens of micrometers. In the second step (as illustrated in Fig. 1**(A)**), the as-grown n-MoS_2/SiO_2/Si from the first step was fed to the CVD furnace to synthesize p-MoS_2 on top of the n-MoS_2 and form a vertically stacked heterostructure (denoted by p-MoS_2/n-MoS_2). In a typical growth condition, the n-MoS_2/SiO_2/Si was loaded into the center of the reaction tube (a 1-in. diameter quartz tube) in the CVD furnace. The n-MoS_2/SiO_2/Si mounted on a quartz plate was positioned against the carrier gas flow in the growth of p-MoS_2 that followed. The growth of the vertically stacked p-MoS_2/n-MoS_2 is challenging, as the p-MoS_2 was produced via an incomplete reduction of the MoO_3 precursor by sulfur at a relatively low growth temperature (530 °C) in the presence of Ar gas. During the reaction, the Ar carrier gas was used to protect the system from oxygen contamination and to carry the sulfur vapor from the upstream chamber in the reaction tube. During the p-MoS_2/n-MoS_2 growth, while the reaction temperature at the MoO_3 zone was maintained at 600 °C, the temperature at the heterostructure forming substrate was set to 530 °C. After the reaction, the morphology of the as-obtained vertical heterostructure of p-MoS_2/n-MoS_2 was examined by OM and atomic force microscopy (AFM). Fig. 1**(D)** shows an OM image of the p-MoS_2/n-MoS_2, in which the optical contrast of the hexagram-shaped structure differentiates the vertically stacked p-MoS_2 (top) and n-MoS_2 (bottom) triangles, and the typical sizes of both MoS_2 triangles are larger than 30 µm. As presented in Fig. 1**(F)**, the bilayer morphology was further verified by AFM imaging, where the AFM topograph of p-MoS_2/n-MoS_2 on a SiO_2/Si substrate has a height of 1.72 nm in the vertically stacked bilayer.

The chemical reaction of the vertically stacked p-MoS_2/n-MoS_2 hexagram is presented in **Eq.** (2) with a plausible formation mechanism given by the following:

$$\text{n-}MoS_2+MoO_3+2S\rightarrow \text{p-}MoOS_2/\text{n-}MoS_2+O_2 \quad (2)$$

For simplicity, we present p-$MoOS_2$ by p-MoS_2 hereafter. The growth of 2D (vertical or lateral) stacking structures can be controlled

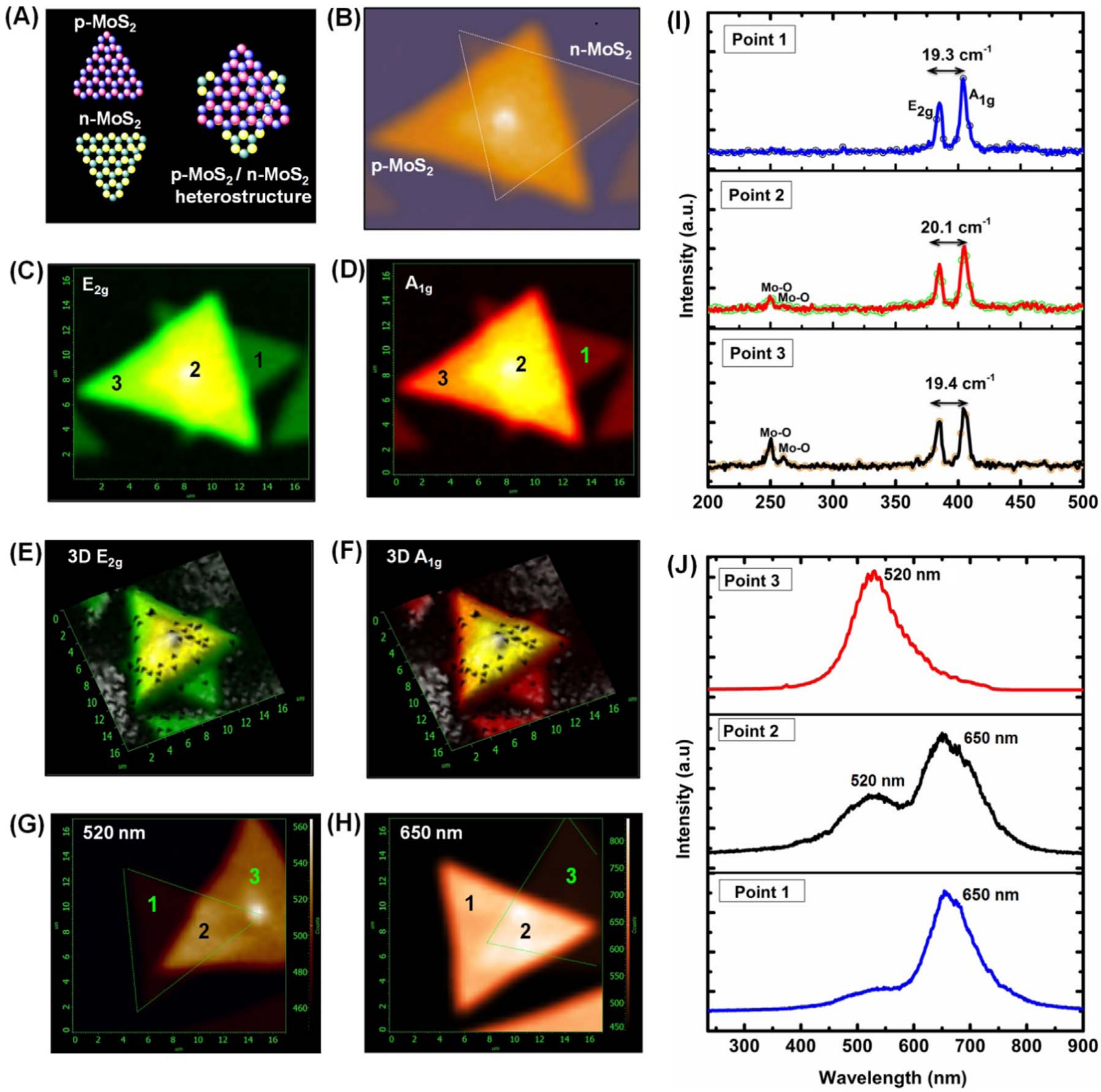

Fig. 2. Raman and PL characterizations of the p-MoS_2/n-MoS_2 heterostructure. (A) Schematic representation of the vertically stacked p-MoS_2/n-MoS_2 heterostructure. (B) OM image of p-MoS_2/n-MoS_2 shows the vertical stacking heterostructure. The edge of the bottom n-MoS_2 is demarcated by white dots. (C–D) E_{2g} and A_{1g} Raman mode mappings of the p-MoS_2/n-MoS_2 heterostructure. (E–F) 3D mappings of the E_{2g} and A_{1g} Raman modes of the p-MoS_2/n-MoS_2 heterostructure. (G–H) PL mappings of the p-MoS_2/n-MoS_2 heterostructure at 520 nm and 650 nm, respectively. The counterpart MoS_2 triangles are demarcated by green dotted lines. (I–J) The Raman and PL spectra of the p-MoS_2/n-MoS_2 heterostructure were measured at three selected points (Points 1–3) as indicated in (C–D) and (G–H), respectively.

by the reaction rate. In our experiment to obtain the vertically stacked p-MoS_2/n-MoS_2, we controlled the reaction rate of the second-step growth using a low-temperature condition, which allowed us to develop vertical stacking instead of lateral stacking or a random formation of alloys. The low temperature growth in the second-step reaction has two advantages. First, the low temperature stopped further growth at the edges of the already-formed n-MoS_2, resulting in the prohibition of a lateral stacking and the facilitation of the vertical growth. Second, the low temperature made the incomplete reduction of MoO_3 possible, consequently producing a p-MoS_2 layer on top of the n-MoS_2.

The as-synthesized bilayer p-MoS_2/n-MoS_2 (schematically illustrated in Fig. 2**(A)**), with an OM image shown in Fig. 2**(B)**, was further confirmed by Raman and PL spectroscopic mappings as displayed in Figs. 2**(C)–(H).** In Raman imaging of the p-MoS_2/n-MoS_2 heterostructure, we performed a single-point 2D Raman mapping using a 488 nm excitation laser (with the power of 20 mW and an exposure time of 1 s) for the in-plane (E_{2g}, at 383 cm^{-1}) and out-of-plane (A_{1g}, at 408 cm^{-1}) Raman modes over a stacked triangular island, as shown in Figs. 2**(C)** and 2**(D)**, respectively [34,35]. It is well known that in the two vertically stacked TMDC triangles grown in parallel on a substrate, the spectral intensity of the out-of-plane A_{1g} mode (408 cm^{-1}) is slightly stronger than that of the in-plane E_{2g} (383 cm^{-1}) mode. The single-point Raman spectral characteristics of the p-MoS_2/n-MoS_2 heterostructure were examined, as displayed in Fig. 2**(I)**, where three specifically selected points (1, 2, and 3) are indicated in Figs. 2**(C)** and 2**(D)**. Point 1 is located on the bottom n-MoS_2 triangle, at which the Raman signals clearly indicate the two A_{1g} (408 cm^{-1}) and E_{2g} (383 cm^{-1}) peaks with the former being slightly stronger. Point 3 is placed on the top p-MoS_2 triangle where, in addition to the A_{1g} and E_{2g} modes, a third peak at 250 cm^{-1} is attributed to the Mo–O stretching. The appearance of this Mo–O stretching mode clearly confirms the existence of the oxygen doping in MoS_2, i.e., an elemental ingredient of the p-MoS_2. More interestingly, Point 2 marks the heterostructure region and exhibits the co-existence of the Raman signals contributed from both n-MoS_2 and p-MoS_2. The Raman features show distinct contributions from individual n-MoS_2 and p-MoS_2 at Point 2 and rule out the formation of an alloy of n-MoS_2 and p-MoS_2 during the synthetic reaction, which would shift the

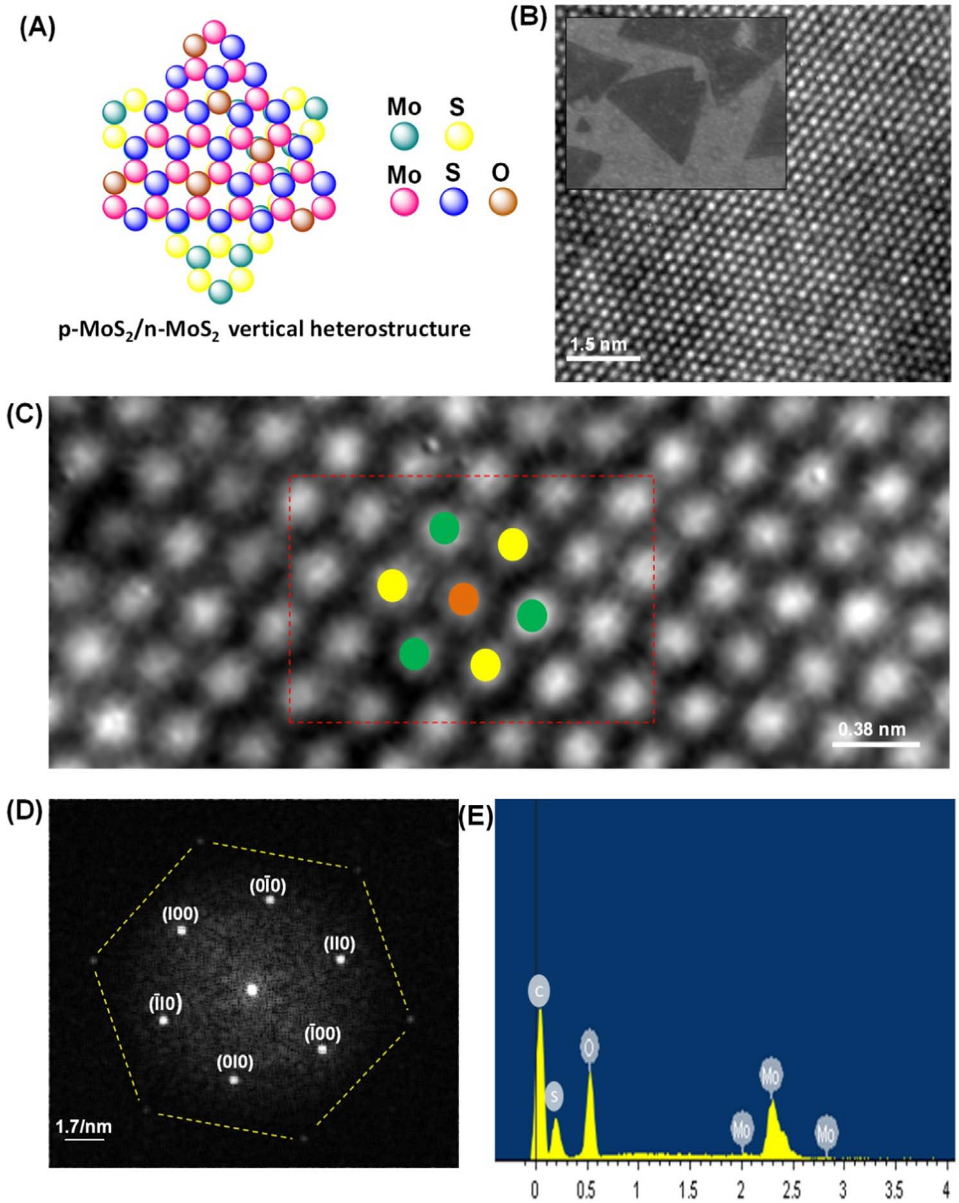

Fig. 3. STEM images for the atomic structure of the p-MoS_2/n-MoS_2 heterostructure. (A) Illustration of the vertically stacked p-MoS_2/n-MoS_2 heterostructure. (B) Low-magnification Z-contrast STEM image of the p-MoS_2/n-MoS_2 heterostructure. The inset shows a magnified SEM image. (C) High-magnification Z-contrast STEM image of the p-MoS_2/n-MoS_2 heterostructure. The positions of Mo and S in n-MoS_2 are represented by the green and yellow colored dots, respectively, and the position of O in p-MoS_2 is represented by the orange colored dot. (D) The SAED pattern obtained from the Fourier transform of the STEM image indicates a hexagonal crystal structure. The SAED pattern shows two bright (hexagonal) rings, corresponding to n-MoS_2 (the inner ring) and p-MoS_2 (the outer ring marked by yellow colored lines). (E) The line-scan EDX spectrum of a selected region from the STEM image (marked by a red color rectangle).

vibrational frequencies of MoS_2 because of the substitution of S by O (in the alloy of n-MoS_2) or the addition of O to Mo (in the alloy of either n-MoS_2 or p-MoS_2). As shown in Fig. 2**(I)**, while the separation of ~19.3 cm^{-1} between the E_{2g} and A_{1g} modes at Point 1 and Point 3 indicates that both n-MoS_2 and p-MoS_2 are present as monolayers [35] (Figs. 2**(C)** and 2**(D)**), the separation of ~20.1 cm^{-1} at Point 2, due to the red shift of the E_{2g} mode and the blue shift of the A_{1g} mode, reveals the vertical stacking of the bilayer p-MoS_2/n-MoS_2 [36], and this bilayer is consistent with the AFM measurement of a height of 1.72 nm (Fig. 1**(F)**). Notably, all of the Raman modes at Points 1–3 in Fig. 2**(I)** belong to the hexagonal (2H) MoS_2, while the Raman modes pertaining to the octahedral (1T) and rhombohedral (3R) coordinations of MoS_2 are absent, indicating that the as-synthesized n-MoS_2, p-MoS_2, and p-MoS_2/n-MoS_2 are all hexagonal (2H) without any structural distortion to the 1T or 3R polytype [37,38]. Moreover, while the uniform, smooth surface of the individual n-MoS_2 and p-MoS_2 can be observed in the 2D Raman mappings of Figs. 2**(C)** and 2**(D)**, the central stacking part (around Point 2) is brighter because of the more intense signals contributed by the p-MoS_2/n-MoS_2 bilayer. To further support our conclusions, we performed 3D Raman mapping for both the E_{2g} and A_{1g} modes to obtain detailed information about the surface homogeneity (Figs. 2**(E)** and 2**(F)**). The obtained 3D Raman scans of the E_{2g} and A_{1g} modes over the stacked region of p-MoS_2/n-MoS_2 clearly show a homogeneous intensity distribution and hence a uniform and smooth surface.

To study the optical features of the heterojunction, we performed the single-point PL measurements over the p-MoS_2/n-MoS_2 bilayer. Figs. 2**(G)** and 2**(H)** depict the PL mapping images, and Fig. 2**(J)** shows the PL spectra of the p-MoS_2/n-MoS_2 excited with a 488 nm laser. The observed PL signals of n-MoS_2 at ~650 nm (1.90 eV, Point 1) and p-MoS_2 at ~520 nm (2.38 eV, Point 3) are attributed to the direct excitonic transitions in the bottom n-MoS_2 and top p-MoS_2, respectively. At Point 2, the PL examined on the p/n stacking bilayer region comprises both ~650 nm and ~520 nm emission signals, providing additional evidence of the van der Waals interaction in the p-MoS_2/n-MoS_2 interlayer without an apparent alloying in the synthetic reaction.

X-ray photoelectron spectroscopy (XPS, Fig. S2) was used to study the chemical compositions of n-MoS_2 and p-MoS_2 with the high-resolution scans in the Mo 3d, O 1s, and S 2p regions. In Fig. S2**(A)**, the n-MoS_2 sample produces the characteristic peaks of a doublet of Mo^{4+}(MoS_2) $3d_{3/2}$ and $3d_{5/2}$ at ~233.0 and ~229.9 eV, respectively, and a singlet of S 2s peak at ~227.2 eV [39,40]. The overall XPS spectra of the p-MoS_2 sample (Fig. S2**(A)**–**(C)**) are similar to those of n-MoS_2, except for the inclusion of an additional doublet peak at ~236.1 and 233.0 eV and a slightly stronger O^{2-} 1s peak located at ~531.0 eV. Moreover, in the spectra of p-MoS_2, the Mo^{4+} state is responsible for the pronounced doublet at ~236.1 and 233.0 eV and the O^{2-} state accounts for the doublet at ~233.0 and ~531.0 eV. These results indicate that the binding of molybdenum is in the form of S–$Mo^{(4+)}$–O, suggesting the existence of the bonded oxygen [41]. The peak at 533.0 eV appearing in both n-MoS_2 and p-MoS_2 is due to the physically adsorbed oxygen molecules (–OH) on the sample surfaces [41,42]. Meanwhile, due to the presence of oxygen bonding in p-MoS_2, the intensities of the $Mo^{4+}3d_{3/2}$ (at ~233.0 eV), $Mo^{4+}3d_{5/2}$ (at ~229.9 eV), and S 2s (at ~227.2 eV) peaks are decreased, but the O^{2-} 1s intensity (at ~531.0 eV) is increased dramatically (Fig. S2**(C)**). The appearance of the higher oxidized Mo^{4+} states (from S–$Mo^{(4+)}$–O) and the increasing oxygen content in the p-MoS_2 sample provide a clear signature of Mo–O bond formation. The fractional percentages of Mo^{4+}(MoS_2), Mo^{4+}(S–$Mo^{(4+)}$–O), S^{2-}, O^{2-}(Mo–O), and O^{2-}(–OH) are summarized in Table S1. Meanwhile, there might also have the Mo=O bond formed (formation of MoO_3) during the p-MoS_2 growth; however, the obtained result did not show an XPS peak for the Mo=O bond (at 530.6 eV) [43,44]. Additionally, the PL result (Fig. 2**(J)**) did not show emission peaks for MoO_3 at 342 nm and 329 nm [43]. The results from both XPS and PL suggest that MoO_3 was not formed during the p-MoS_2 growth.

To gain insight into the electronic structures of the bilayer p-MoS_2/n-MoS_2 heterojunction, we conducted experiments by UPS. As depicted in Fig. S1**(A)** and described in Supporting information Section S1, the work functions (ϕ) of both n-MoS_2 and p-MoS_2 can be calculated from the observed UPS spectral data. The secondary electron cutoffs for n-MoS_2 and p-MoS_2 in the UPS spectra are observed to be 17 and 16.5 eV, respectively (Figs. S1**(B)** and S1**(C)**). The work functions for n-MoS_2 and p-MoS_2 were calculated to be 4.6 and 5.1 eV, respectively (details in Supporting information Section S1). This result shows that the incomplete reduction in the growth of p-MoS_2 made the work function of p-MoS_2 increase from 4.6 eV (of n-MoS_2) to 5.1 eV, also demonstrating the change of n-MoS_2 to p-MoS_2. Based on the above analyses, we have constructed an energy diagram (Fig. 4**(B)**) aligning the relative band positions of the bilayer p-MoS_2/n-MoS_2 heterojunction.

Fig. 3 shows the atomic-resolution Z-contrast scanning transmission electron microscopic (STEM) images of the p-MoS_2/n-MoS_2 heterostructure. The hexagonal lattices of both p-MoS_2 and n-MoS_2 in the stacking region (Fig. 3**(A)**) are oriented such that the most stable crystal structure is achieved with the minimum energy. Displayed in Figs. 3**(B)** and 3**(C)** are the low- and high-magnification STEM images for the vertically stacked heterostructures, clearly showing the van der Waals stacking between p-MoS_2 and n-MoS_2. The selected-area electron diffraction (SAED) pattern **(**Fig. 3**(D))** from the Fourier transform of the STEM image confirmed that the interplanar distance (d) in p-MoS_2/n-MoS_2 heterostructure is d=0.28 nm, which match the [100] facet of MoS_2. Also, the angle between the [010] and [100] planes is 120°, which reveals a hexagonal lattice structure. The SAED pattern (Fig. 3**(D)**) can also be used to determine the stacking pattern and stacking layer number, where the two bright (hexagonal) rings indicate the vertical 2H stacking phase between the two single layers of p-MoS_2 and n-MoS_2. An EDX (Fig. 3**(E)**) spectral analysis further identified the p-MoS_2/n-MoS_2 heterostructure to have Mo, S, and O as the principal elemental components (the C peak is from the carbon-coated TEM grid), consistent with the XPS examination **(**Fig. S2**)**.

For an optoelectronic application, we designed a WLED using n-MoS_2, p-MoS_2, and p-GaN as the orange, green, and blue emitters, respectively. As illustrated in Fig. S3**(A)**, the p-GaN was grown on a c-face sapphire substrate (denoted as p-GaN/sapphire). In our experiment, we used bilayered (2-L) p-GaN because the indirect band gap of 1-L p-GaN transforms to a direct band gap in 2-L p-GaN to have strong PL/EL [45]. The detailed procedures for the 2-L p-GaN growth are given in Supporting Information Section 3. Fig. S3**(C)** shows an AFM image of the as-grown p-GaN nanosheets with a thickness of ~0.56 nm, which corresponds to a 2-L p-GaN. The crystalline quality of the 2-L p-GaN was investigated by confocal Raman spectroscopy, as displayed in Fig. S3**(D)**, showing the strong E_2 band at 588 cm^{-1} and the weak A_1 band at 753 cm^{-1} with an intensity ratio of $I_{A1}/I_{E2} < 1$ and confirming the as-synthesized p-GaN to be of high crystalline quality [46]. After the growth of p-GaN/sapphire, a dielectric SiO_2 layer (20 nm thick) was sputtered on about one-third of the area of the p-GaN/sapphire for the later deposition of an electrode (50 nm Au/2 nm Cr) for electric measurements (as illustrated in Fig. 4**(A)**). The leakage current (I_{gate}) of the 20 nm thick SiO_2 dielectric layer was tested by sweeping the gate bias from −8 to 8 V. As shown in Fig. S4, the measured leakage currents are very small and at the noise level within the gate bias of ± 8 V. Subsequently, the vertically stacked p-MoS_2/n-MoS_2 heterostructure was transferred onto the p-GaN/SiO_2 surface to reside partly on the p-GaN surface and partly on the SiO_2 dielectric layer. The vertically

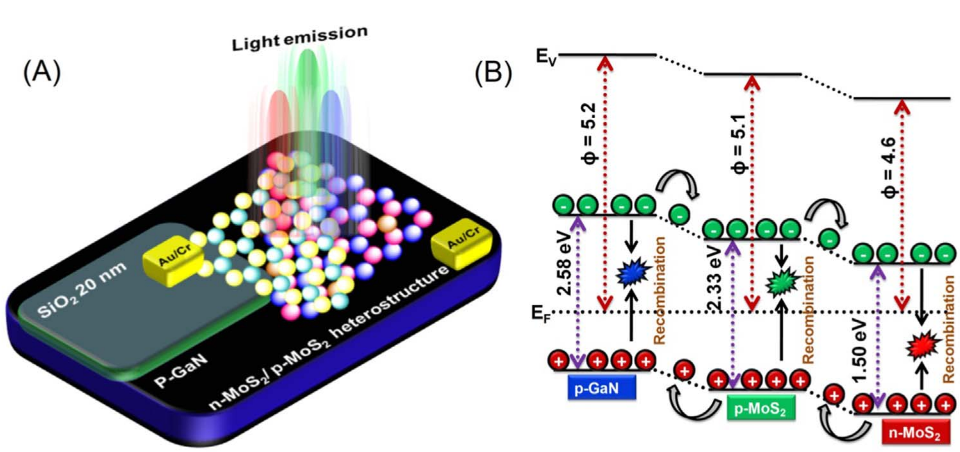

Fig. 4. A WLED device with the 4-L n-MoS_2/p-MoS_2/p-GaN heterostructure.(A) Schematic illustration of the WLED device constructed by three emitters in the n-MoS_2/p-MoS_2/p-GaN. (B) The band alignment of the vertically stacked n-MoS_2/p-MoS_2/p-GaN heterostructure with the band energies obtained from the UPS analysis.

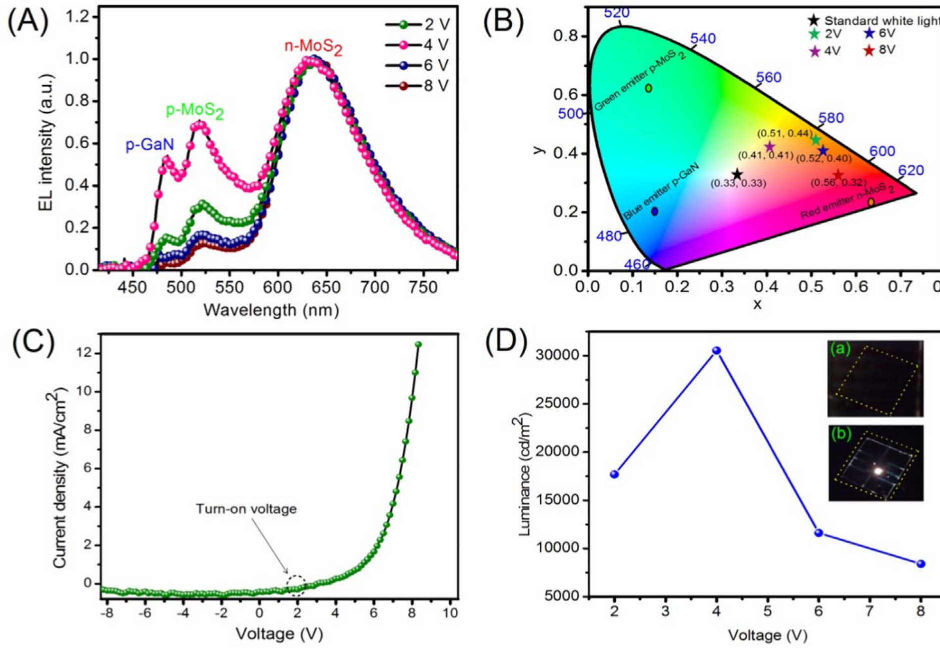

Fig. 5. Optical and electrical measurements of the 4-L n-MoS_2/p-MoS_2/p-GaN WLED device. (A) EL spectra were observed from the WLED device of n-MoS_2/p-MoS_2/p-GaN as a function of the applied forward bias from 2 to 8 V. The EL spectra comprise three emissions in the blue (481 nm), green (525 nm), and orange (642 nm) regions from p-GaN, p-MoS_2, and n-MoS_2, respectively. (B) The color purity of the emitted light from the n-MoS_2/p-MoS_2/p-GaN device at each bias voltage from 2 to 8 V is represented by the CIE color coordinates. (C) The current-voltage characteristics (I-V) of the n-MoS_2/p-MoS_2/p-GaN device were measured by applying a positive bias on n-MoS_2 and the electrode on p-GaN was grounded. (D) The luminescence characteristics of the WLED device at different biasing conditions were investigated, where the maximum luminescences of 17,677, 30,548, 11,612, and 8389 cd/m^2 were observed at the bias voltages of 2, 4, 6, and 8 V, respectively. A dark image at zero bias and a white light emission image at 4 V of the WLED device are shown in the inset. The device boundary is demarcated by yellow dotted lines.

stacked heterostructure was transferred with an etching-free transfer process by polydimethylsiloxane (PDMS) stamping. After the p-MoS_2/n-MoS_2 was stamped on the p-GaN/SiO_2 surface, this vertically stacked device was sonicated in deionized water at 90 °C for 1 h, resulting in the detachment of the p-MoS_2/n-MoS_2 hexagram from the PDMS stamp by intercalating water into the PDMS–SiO_2 interface. Following the formation of the n-MoS_2/p-MoS_2/p-GaN heterostructure, a pair of contact electrodes was fabricated on both p-GaN and n-MoS_2 by thermal evaporation of Au (50 nm) with an adhesion layer of Cr (2 nm).

Fig. 5(A) shows the EL measurements of the as-fabricated n-MoS_2/p-MoS_2/p-GaN device performed in forward bias from 2 to 8 V. The observed EL spectrum consists of three emissions of blue (from p-GaN), green (from p-MoS_2), and orange (from n-MoS_2) to serve as the white-light emitting constituents. To understand the emitting mechanism, we applied different bias voltages and found that the n-MoS_2/p-MoS_2/p-GaN heterojunction can display an EL under forward bias. In Fig. 5**(A)**, when the bias voltage increases from 2 to 4 V, an enhancement in the EL was observed. However, when the applied voltage was higher than 4 V, the EL declined; this was likely due to the breakdown of the n-MoS_2/p-MoS_2/p-GaN heterojunction. The white-light emission from the vertically stacked device can be interpreted with the help of an energy-band alignment of the n-MoS_2, p-MoS_2, and p-GaN emitting constituents, as displayed in Fig. 4**(B)**. In forward bias, while the injected holes (from the drain electrode) in the valence bands (VB) could transfer from n-MoS_2 to p-MoS_2, and later to p-GaN, the injected electrons (from the source electrode) in the conduction bands (CB) could migrate from p-GaN to p-MoS_2 and finally to n-MoS_2. During the charge-carrier transfer, the electron-hole recombination could take place at p-GaN, p-MoS_2, and n-MoS_2 to yield the emissions at ~481, ~525, and ~642 nm, respectively. The CIE color coordinates of an LED device were determined with a commercially available software and are presented in Fig. 5**(B)**. The device operated at 4 V showed the white color purity of CIE (0.41, 0.41), which is very close to the standard white light of CIE (0.33, 0.33). The white light emission at 4 V is mainly due to the moderate increases of the blue and green light emissions in the EL spectra (as shown in Fig. 5**(A)**). In the colorimetry, the LEDs of any emission color in the quadrangle can be obtained by mixing different emission color composites. By combining the blue (~481 nm of p-GaN), green (~525 nm of p-MoS_2), and orange (~642 nm of n-MoS_2) emissions from the n-MoS_2/p-MoS_2/p-GaN heterostructure, the potential to fabricate atomically thin light sources with white-light emission has been demonstrated clearly from the observed EL and CIE (Figs. 5**(A)** and 5**(B)**). The electrical characteristics of the WLED device were investigated by measuring the current-voltage (*I-V*) curve from −8 to +8 V as shown in Fig. 5**(C)**, where a low turn-on voltage of 2 V was observed. (A turn-on voltage is defined as the lowest possible voltage required to turn the LED device on and the current increases rapidly at the bias above the turn-on voltage.) In addition, we measured the luminescence characteristics of the WLED device at different biasing conditions as shown in Fig. 5**(D).** It is noted that the n-MoS_2/p-MoS_2/p-GaN device operated at 4 V acquire the maximum luminance of 30,548 cd/m^2, in comparison with those of 17,677, 11,612, and 8389 cd/m^2 operated at the biases of 2 ,6, and 8 V, respectively. To evaluate the illuminating performance of the as-fabricated WLED device, we have calculated the luminescence efficiency (η) and luminous efficacy (μ). While the luminous efficiency (η) is defined as the ratio of luminous flux to electric power, the luminous efficacy (μ) is defined as the ratio of luminous flux to optical power.

$$\eta \quad = \frac{\phi v}{Electrical\ Power} = \frac{Km \int_{380}^{780} \phi e\,[\lambda]\,V\,[\lambda]\,d\lambda}{IV} \tag{3}$$

$$\mu = \frac{\phi v}{Optical\ Power} = \frac{Km \int_{380}^{780} \phi e\,[\lambda]\,V\,[\lambda]\,d\lambda}{\int_{380}^{780} \phi e\,[\lambda]} \tag{4}$$

In Eq. (3), ϕv is the luminous flux, Km is the maximum spectral luminance efficiency, (Φe[λ]) is the radiometric power, and (V[λ]dλ) is the standard luminous efficiency coefficient. The WLED device operated at 4 V showed aluminous efficiency of 29% and a luminous efficacy of 294 lm/W. The detailed calculations for the luminous efficacy are given in Supporting information Section 5.

4. Conclusion

We report, for the first time, white light emission from a vertically stacked heterostructure of three constituent emitters composed of 1-L n-MoS_2, 1-L p-MoS_2, and 2-L p-GaN. The EL spectra obtained from this 4-L WLED device of the n-MoS_2/p-MoS_2/p-GaN heterostructure clearly exhibited three emission peaks from n-MoS_2 (orange at ~642 nm), p-MoS_2 (green at ~525 nm), and p-GaN (blue at ~481 nm) in forward bias, with the dominant emission at ~642 nm from n-MoS_2. The as-fabricated n-MoS_2/p-MoS_2/p-GaN device showed a maximum luminance of 30,548 cd/m^2 at the forward bias of 4 V. This WLED device holds great potential for constructing color-tunable light emitters for low-cost display, lighting, and optical communication by using the burgeoning 2D materials-based optoelectronic nanotechnology.

Acknowledgements

This work was partially supported by the Ministry of Science and Technology, Taiwan under the grant numbers of MOST 104–2627-M-002-002 and MOST 103–2113-M-002–014-MY3.

Appendix A. Supplementary material

Supplementary data associated with this article can be found in the online version at doi:10.1016/j.nanoen.2017.01.006.

References

[1] X. Duan, C. Wang, A. Pan, R. Yu, X. Duan, Chem. Soc. Rev. 44 (2015) 8859–8876.
[2] K.F. Mak, J. Shan, Nat. Photon 10 (2016) 216–226.
[3] Y. Liu, N.O. Weiss, X. Duan, H.-C. Cheng, Y. Huang, X. Duan, Nat. Rev. Mater. (2016) 16042.
[4] N. Choudhary, J. Park, J.Y. Hwang, H.-S. Chung, K.H. Dumas, S.I. Khondaker, W. Choi, Y. Jung, Sci. Rep. 6 (2016) 25456.
[5] X. Li, H. Zhu, J. Mater. 1 (2015) 33–44.
[6] F. Withers, O. Del Pozo-Zamudio, A. Mishchenko, A.P. Rooney, A. Gholinia, K. Watanabe, T. Taniguchi, S.J. Haigh, A.K. Geim, A.I. Tartakovskii, K.S. Novoselov, Nat. Mater. 14 (2015) 301–306.
[7] S.H. Song, B.H. Kim, D.-H. Choe, J. Kim, D.C. Kim, D.J. Lee, J.M. Kim, K.J. Chang, S. Jeon, Adv. Mater. 27 (2015) 3152–3158.
[8] D.O. Scanlon, G.W. Watson, D.J. Payne, G.R. Atkinson, R.G. Egdell, D.S.L. Law, J. Phys. Chem. C 114 (2010) 4636–4645.
[9] T. Pulli, T. Donsberg, T. Poikonen, F. Manoocheri, P. Karha, E. Ikonen, Light Sci. Appl. 4 (2015) e332.
[10] O. Graydon, Nat. Photon 7 (2013) (585-585).
[11] M.A. Schreuder, K. Xiao, I.N. Ivanov, S.M. Weiss, S.J. Rosenthal, Nano Lett. 10 (2010) 573–576.
[12] C. Wang, R. Bao, K. Zhao, T. Zhang, L. Dong, C. Pan, Nano Energy 14 (2015) 364–371.
[13] N. Bano, S. Zaman, A. Zainelabdin, S. Hussain, I. Hussain, O. Nur, M. Willander, J. Appl. Phys. 108 (2010) 043103.
[14] J.K. Park, C.H. Kim, S.H. Park, H.D. Park, S.Y. Choi, Appl. Phys. Lett. 84 (2004) 1647–1649.
[15] P. Pust, V. Weiler, C. Hecht, A. Tücks, A.S. Wochnik, A.-K. Henß, D. Wiechert, C. Scheu, P.J. Schmidt, W. Schnick, Nat. Mater. 13 (2014) 891–896.
[16] T.M. Tolhurst, T.D. Boyko, P. Pust, N.W. Johnson, W. Schnick, A. Moewes, Adv. Opt. Mater. 3 (2015) 546–550.
[17] R. Zhang, H. Lin, Y. Yu, D. Chen, J. Xu, Y. Wang, Laser Photonics Rev. 8 (2014) 158–164.
[18] J. McKittrick, L.E. Shea-Rohwer, J. Am. Ceram. Soc. 97 (2014) 1327–1352.
[19] H. Daicho, T. Iwasaki, K. Enomoto, Y. Sasaki, Y. Maeno, Y. Shinomiya, S. Aoyagi, E. Nishibori, M. Sakata, H. Sawa, S. Matsuishi, H. Hosono, Nat. Commun. 3 (2012) 1132.
[20] I.-H. Lee, L.-W. Jang, A.Y. Polyakov, Nano Energy 13 (2015) 140–173.
[21] H. Uoyama, K. Goushi, K. Shizu, H. Nomura, C. Adachi, Nature 492 (2012) 234–238.
[22] S. Wang, X. Wang, B. Yao, B. Zhang, J. Ding, Z. Xie, L. Wang, Sci. Rep. 5 (2015) 12487.
[23] B. Liu, H. Tao, L. Wang, D. Gao, W. Liu, J. Zou, M. Xu, H. Ning, J. Peng, Y. Cao, Nano Energy 26 (2016) 26–36.
[24] M.U. Hassan, Y.-C. Liu, Ku Hasan, H. Butt, J.-F. Chang, R.H. Friend, Nano Energy 21 (2016) 62–70.
[25] R.S. Sundaram, M. Engel, A. Lombardo, R. Krupke, A.C. Ferrari, P. Avouris, M. Steiner, Nano Lett. 13 (2013) 1416–1421.
[26] Y. Rong, Y. Sheng, M. Pacios, X. Wang, Z. He, H. Bhaskaran, J.H. Warner, ACS Nano 10 (2016) 1093–1100.
[27] M.-Y. Li, Y. Shi, C.-C. Cheng, L.-S. Lu, Y.-C. Lin, H.-L. Tang, M.-L. Tsai, C.-W. Chu, K.-H. Wei, J.-H. He, W.-H. Chang, K. Suenaga, L.-J. Li, Science 349 (2015) 524–528.
[28] C. Huang, S. Wu, A.M. Sanchez, J.J.P. Peters, R. Beanland, J.S. Ross, P. Rivera, W. Yao, D.H. Cobden, X. Xu, Nat. Mater. 13 (2014) 1096–1101.
[29] X.-Q. Zhang, C.-H. Lin, Y.-W. Tseng, K.-H. Huang, Y.-H. Lee, Nano Lett. 15 (2015) 410–415.
[30] K. Bogaert, S. Liu, J. Chesin, D. Titow, S. Gradečak, S. Garaj, Nano Lett. 16 (2016) 5129–5134.
[31] Y. Gong, J. Lin, X. Wang, G. Shi, S. Lei, Z. Lin, X. Zou, G. Ye, R. Vajtai, B.I. Yakobson, H. Terrones, M. Terrones, Beng K. Tay, J. Lou, S.T. Pantelides, Z. Liu, W. Zhou, P.M. Ajayan, Nat. Mater. 13 (2014) 1135–1142.
[32] G. Clark, J.R. Schaibley, J. Ross, T. Taniguchi, K. Watanabe, J.R. Hendrickson, S. Mou, W. Yao, X. Xu, Nano Lett. 16 (2016) 3944–3948.
[33] X. Wang, F. Xia, Nat. Mater. 14 (2015) 264–265.
[34] H. Li, Q. Zhang, C.C.R. Yap, B.K. Tay, T.H.T. Edwin, A. Olivier, D. Baillargeat, Adv. Funct. Mater. 22 (2012) 1385–1390.
[35] C. Lee, H. Yan, L.E. Brus, T.F. Heinz, J. Hone, S. Ryu, ACS Nano 4 (2010) 2695–2700.
[36] R. Saito, Y. Tatsumi, S. Huang, X. Ling, M.S. Dresselhaus, J. Phys.: Condens. Matter 28 (2016) 353002.
[37] Y. Guo, D. Sun, B. Ouyang, A. Raja, J. Song, T.F. Heinz, L.E. Brus, Nano Lett. 15 (2015) 5081–5088.
[38] J.-U. Lee, K. Kim, S. Han, G.H. Ryu, Z. Lee, H. Cheong, ACS Nano 10 (2016) 1948–1953.
[39] R. Kappera, D. Voiry, S.E. Yalcin, B. Branch, G. Gupta, A.D. Mohite, M. Chhowalla, Nat. Mater. 13 (2014) 1128–1134.
[40] R.D. Nikam, A.-Y. Lu, P.A. Sonawane, U.R. Kumar, K. Yadav, L.-J. Li, Y.-T. Chen, ACS Appl. Mater. Interfaces 7 (2015) 23328–23335.
[41] L. Tao, X. Duan, C. Wang, X. Duan, S. Wang, Chem. Commun. 51 (2015) 7470–7473.
[42] H. Nan, Z. Wang, W. Wang, Z. Liang, Y. Lu, Q. Chen, D. He, P. Tan, F. Miao, X. Wang, J. Wang, Z. Ni, ACS Nano 8 (2014) 5738–5745.
[43] N. Illyaskutty, S. Sreedhar, G. Sanal Kumar, H. Kohler, M. Schwotzer, C. Natzeck, V.P.M. Pillai, Nanoscale 6 (2014) 13882–13894.
[44] W. Xuan, Z. Yong Ping, C. Zhi Qian, Mater. Res. Express 3 (2016) 065014.
[45] Y. Mu, J. Phys. Chem. C 119 (2015) 20911–20916.
[46] A. Hoffmann, A. Kaschner, C. Thomsen, Physica Status Solidi (C) 0 (2003) 1783–1794.

Revannath Dnyandeo Nikam obtained his Ph.D. degree in chemistry at National Taiwan University in collaboration with the TIGP Nano Science & Technology Program at Academia Sinica, Taiwan. His research interests are focused on the themes of 2D materials, such as to synthesize new monolayer single-crystalline 2D materials using an advanced chemical vapor deposition (CVD) technique, to fabricate heterostructures from the synthesized 2D materials, to analyze the newly grown 2D materials, and to explore the electronic and structural properties of the 2D materials-based devices for various applications in light emitting diodes (LED), fuels cells, and electro-catalysis for hydrogen and oxygen evolution reactions (HER and OER).

Poonam Ashok Sonawane received her B.S. and M.S. degrees from Pune University. She is now pursuing her Ph.D. degree in chemistry at National Chiao-Tung University in collaboration with the TIGP Sustainable Chemical Science & Technology Program at Academia Sinica, Taiwan. Her current researches are focused on the fundamental study of organic electronics, including organic light emitting diodes (OLEDs), organic photodetectors, organic solar cells, organic transistors, and the applications of these organic devices.

Raman Sankar is a joint senior postdoctoral research fellow at both Center for Condensed Matter Sciences, National Taiwan University and Institute of Physics, Academia Sinica, Taiwan. He received his Ph.D. in physics from Anna University in 2007. His research is focused on investigating and perfecting the single-crystal growths of 1D and 2D materials for electronic uses. He has published more than 100 papers in high-profile international journals and won numerous prestigious awards.

Yit-Tsong Chen is a Professor and Chair in the Chemistry Department of National Taiwan University. He is also an adjunct Research Fellow at the Institute of Atomic and Molecular Sciences, Academia Sinica in Taiwan. He joined the faculties in 1991 after receiving his B.S. degree from National Taiwan University (1980) and Ph.D. degree from the University of Chicago (1988) and having postdoctoral research training at MIT (1989–1991). In his early research career, he was interested in studies of the superfine structures, vibrational dynamics, and Rydberg states of fundamental molecules using a variety of nonlinear laser optics. In the late 1990s, fascinated by the nanoscale world, he shifted part of his research to catalytic growth and spectroscopic characterization of nanoparticles and nanowires. His current research interests are focused on the application of nanowire field-effect transistor-based biosensors for biological studies and the catalytic synthesis and architectural design of 2D materials for optoelectronic, energy conversion/storage, and biosensing applications.

Supporting Information

Epitaxial Growth of Vertically Stacked p-MoS_2/n-MoS_2 Heterostructures by Chemical Vapor Deposition for Light Emitting Devices

Revannath Dnyandeo Nikam[1,2,3], Poonam Ashok Sonawane[4,5,6], Raman Sankar[7,8], and Yit-Tsong Chen[1,2,*]

[1]Department of Chemistry, National Taiwan University, Taipei 106, Taiwan

[2]Institute of Atomic and Molecular Sciences, Academia Sinica, Taipei 106, Taiwan

[3]Nanoscience and Technology Program, Taiwan International Graduate Program, Academia Sinica, Taipei 115, Taiwan

[4]Institute of Chemistry, Academia Sinica, Taipei 115, Taiwan

[5]Department of Applied Chemistry, National Chiao-Tung University, Hsinchu 300, Taiwan

[6]Sustainable Chemical Science and Technology Program, Taiwan International Graduate Program, Academia Sinica, Taipei 115, Taiwan

[7]Center for Condensed Matter Sciences, National Taiwan University, Taipei 10617, Taiwan

[8]Institute of Physics, Academia Sinica, Taipei 10617, Taiwan

[*]*Address correspondence to: ytcchem@ntu.edu.tw*

S1. Calculation of the work functions of n-MoS_2 and p-MoS_2

The work functions for both n-MoS_2 and p-MoS_2 were calculated from the observed UPS spectra as shown in **Figs. S1(B)** and **S1(C)**, respectively. For the UPS measurements, the He I radiation line at 21.6 eV from a discharge lamp was used. The onset and cutoff values were calculated from the observed UPS spectra using a standard procedure for determining the work function (ϕ). As the energy diagram depicted in **Fig. S1(A)**, the kinetic energy (K_{kin}) of an ejected photoelectron from the sample surface under illumination ($h\nu$) is expressed as[S1]

$$E_{kin} = h\nu - \phi - E_b, \qquad \textbf{[Eq. 1]}$$

Where $h\nu$ is the photon energy, ϕ is the work function of the sample, E_b is the binding energy of the ejected electron. In the observed UPS spectra, the fastest ejected photoelectrons will be the primary electrons emitted directly from the Fermi edge and thus E_b=0.

At the onset ($E_{b\,(onset)}$=0), $\phi = h\nu - E_{kin}$, **[Eq. 2]**

which corresponds to the Fermi energy (E_F). On the other hand, the ejected electrons close to the secondary electron cutoff edge are the slowest electrons, which have nearly zero kinetic energy (E_{kin} = 0) after leaving the sample surface.

At the cutoff edge (E_{kin}=0), $\phi = h\nu - E_{b\,(cutoff)}$. **[Eq. 3]**

In the UPS spectra of n-MoS_2 and p-MoS_2 (**Fig. S1(B)** and **S1(C)**), energies of the cutoff edges were observed to be $E_{b\,(cutoff)}$ = 17 eV and 16.5 eV, respectively. With $h\nu$ =21.6 eV, we obtained

$$\phi_{n\text{-}MoS_2} = 4.6 \text{ eV} \qquad \textbf{[Eq. 4]}$$

and

$$\phi_{p\text{-}MoS_2} = 5.1 \text{ eV}. \qquad \textbf{[Eq. 5]}$$

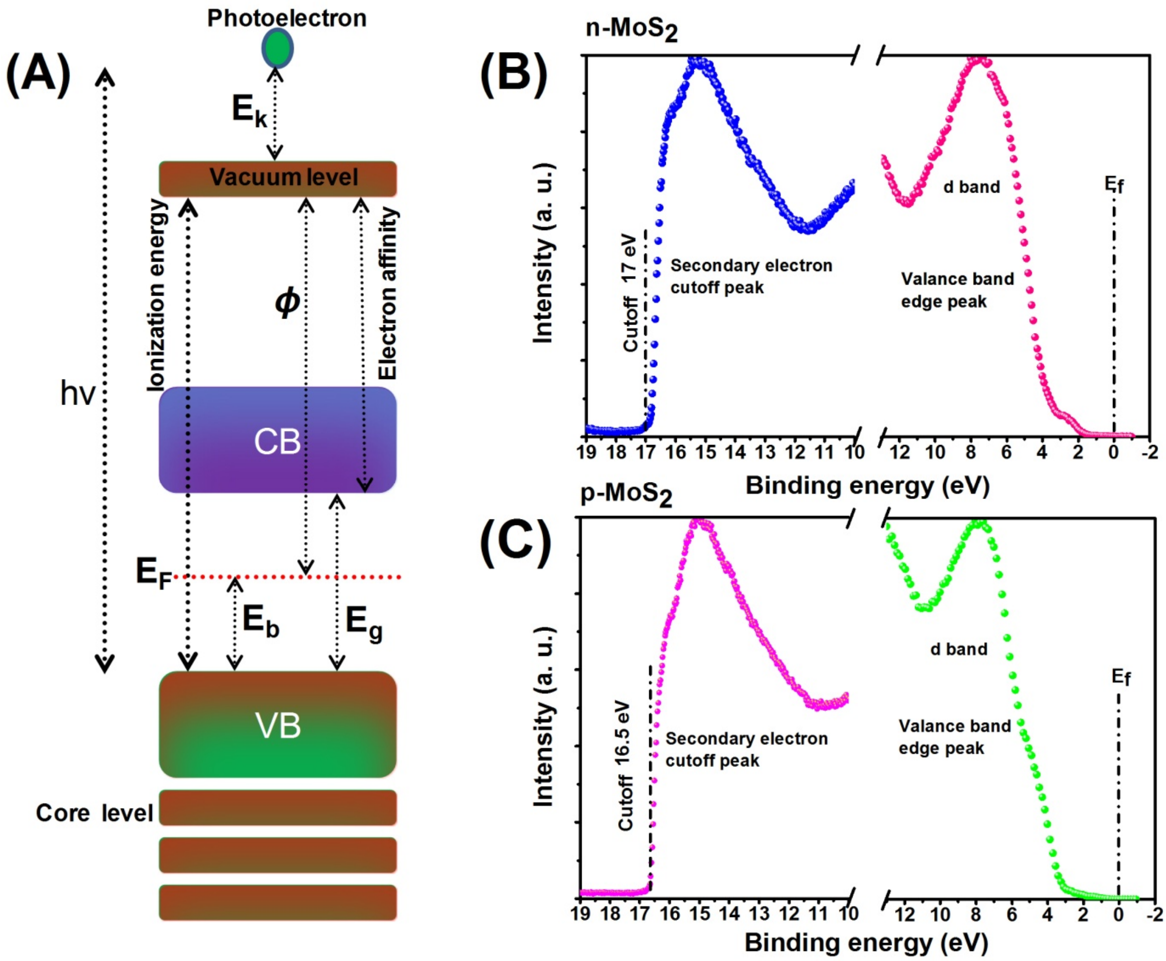

Fig. S1. (A) Schematic representation of the energy diagram related with the observations by UPS spectroscopy. E_b: binding energy, E_f: Fermi energy, E_g: band gap energy, E_k: kinetic energy of an escaped electron, ϕ: work function. (B−C) The UPS spectra of (B) n-MoS_2 and (C) p-MoS_2 were observed, where the binding energies at the cutoff edge are determined to be 17 eV and 16.5 eV, respectively.

S2. XPS spectra of n-MoS_2 and p-MoS_2

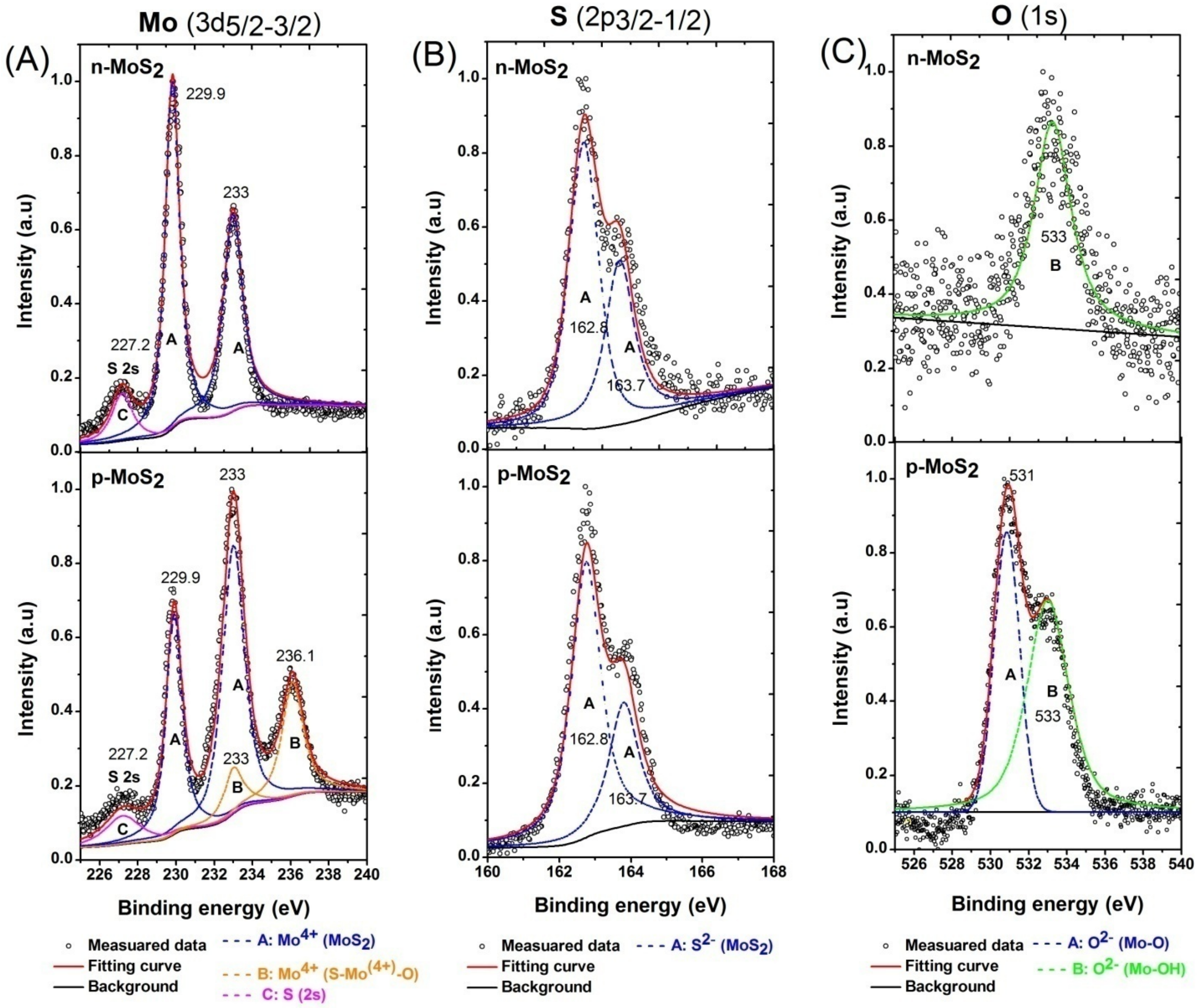

Fig. S2. (A–C) High-resolution XPS spectra of Mo 3d, S 2p, and O 1s for n-MoS_2 and p-MoS_2. In both samples, S 2p shows a doublet of $2p_{3/2}$ and $2p_{1/2}$ at163.7 eV and 162.8 eV, respectively. Mo 3d exhibits a doublet of $3d_{5/2}$ and $3d_{3/2}$ at 229.9 eV and 233.0 eV, respectively. S 2s is located at 227.2 eV. However, for p-MoS_2, Mo 3d possesses additional doublet peaks at 236.1 eV and 233.0 eV, which belong to S–$Mo^{(4+)}$–O. In the O 1s spectral region, a low-intensity peak at 533.0 eV, attributed to the adsorbed oxygen on the sample surface, appeared in both the XPS spectra of n-MoS_2 and p-MoS_2. In contrast, a peak at 531.0 eV, due to existence of the S–$Mo^{(4+)}$–O bond, only appeared in p-MoS_2.

Table S1. Summary of the analyzed data from the XPS spectra shown in Fig. S2

Region		n- MoS_2				p- MoS_2			
		Position (eV)	**FWHM (eV)**	**Normalized area**	**Fraction (%)**	**Position (eV)**	**FWHM (eV)**	**Normalized area**	**Fraction (%)**
Mo3d	**Mo^{+4} $3d_{5/2}$ (MoS_2)**	229.9	0.89	1.22	32.91	229.9	0.98	0.85	26.11
	Mo^{+4} $3d_{3/2}$ (MoS_2)	233.0	089	0.92		233.0	0.98	0.87	
	Mo^{+4} $3d_{5/2}$ (Mo-O)	No	No	No	No	233.0	0.231.20	0.54	14.28
	Mo^{+4} $3d_{3/2}$ (Mo-O)	No	No	No		236.1	0.23	0.63	
	S 2s	227.2	0.31	0.24	9.75	227.2	0.29	0.22	8.94
S 2p	**S^{2-} $2p_{1/2}$**	163.7	0.97	0.20	54.24	163.7	0.94	0.19	43.20
	S^{2-} $2p_{3/2}$	162.8	0.97	0.43		162.8	0.94	0.39	
O 1s	**O^{2-} 1s**(–OH)	533	0.67	0.47	3.10	533	0.65	0.43	2.21
	O^{2-} 1s (Mo–O)	No	No	No	No	531	0.70	0.87	5.26

The fractional percentage of S is calculated from the formula of S^{2-} (%) = (the areas under the S^{2-} $2p_{3/2}$ and S^{2-} $2p_{1/2}$ peaks)/(the sensitivity factor of S^{2-}) ×100. The same method was applied to calculate the fractional percentages of Mo and O.

S3. Epitaxial growth of 2-L p-GaN in CVD reaction

The 2-L p-GaN single crystals were synthesized in a CVD reaction, where a pure Ga metal and ammonia (NH_3) gas were applied as reaction precursors. A c-face sapphire was used as a growth substrate. Before the reaction started, the growth substrate was cleaned sequentially in deionized (DI) water, methyl alcohol, and a heated solution of 3:1 H_2SO_4:H_2O_2, and it was finally rinsed in DI water. The Ga precursor and the sapphire substrate were fed to a CVD furnace. In the synthetic reaction, while the temperature at the Ga precursor was maintained at 600 °C, the growth substrate was heated to 1070 °C. In the growth process, the system was first evacuated to ~100 mTorr without introducing carrier gas (**Fig. S3**). Pure ammonia (NH_3) and hydrogen (H_2) gases were used as the nitrogen source and a reducing agent, respectively. During the growth of 2-L p-GaN, the pressure in the reaction system was maintained at 1 Torr with 100 sccm H_2 and 500 sccm NH_3.

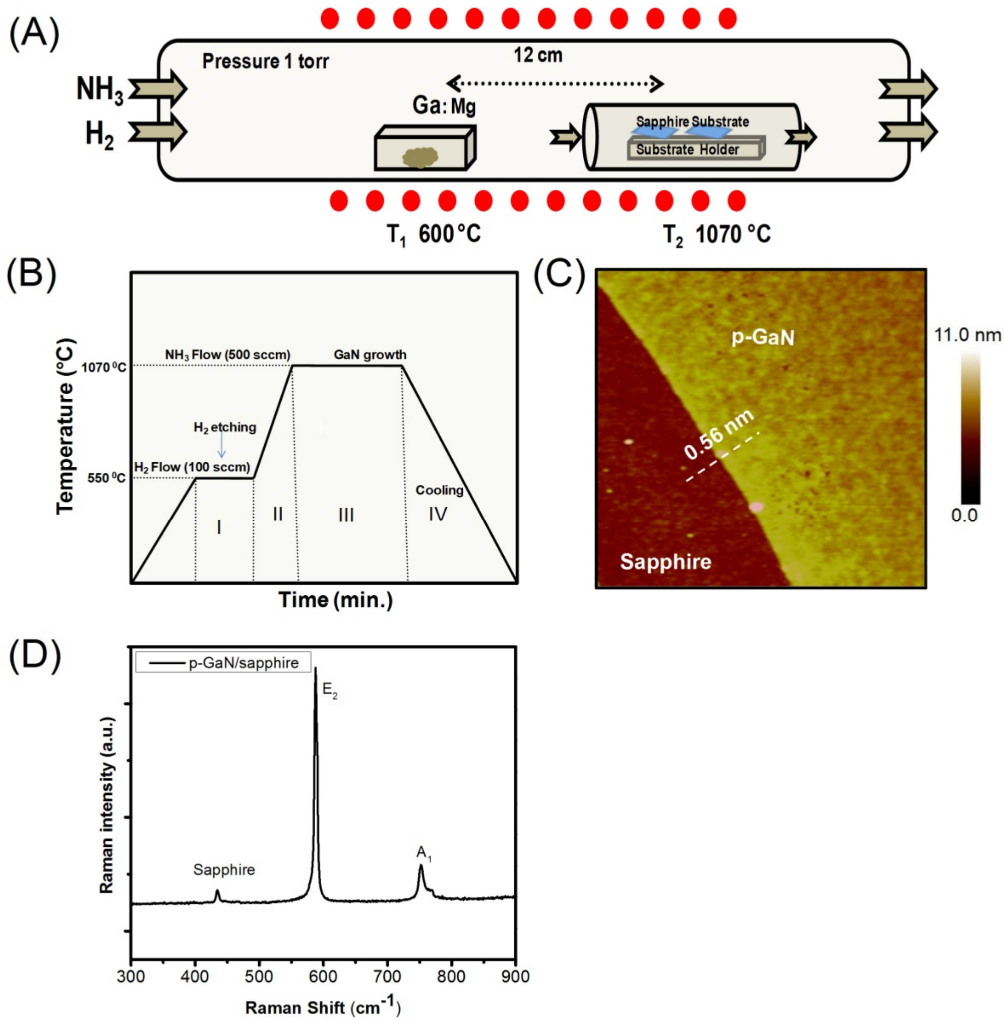

Fig. S3. (A) The experimental setup for the CVD growth of 2-L p-GaN, where T_1 (600 °C) and T_2 (1070 °C) represent the temperatures at the locations of the Ga precursor and the sapphire growth substrate, respectively. (B) The temperature profile of the multi-step protocol for the growth of 2-L p-GaN single crystals. (C) AFM image of a 2-L p-GaN on a sapphire substrate and the thickness of the 2-L p-GaN is ~0.56 nm, as determined from the AFM cross sectional profile. (D) The observed Raman spectra of the as-grown p-GaN on a sapphire substrate show the strong E_2 band at 588 cm^{-1} and the weak A_1 band at 753 cm^{-1}. The sapphire substrate is responsible for the very weak peak at 435 cm^{-1}.

S4. Test of the leakage current

An insulating layer of SiO_2 has been commonly used as a dielectric layer in 2D materials-based LED devices[S2]. In our device fabrication, we deposited a 20 nm-thick SiO_2 layer by sputtering as an insulating layer. In the following **Fig. S4**, we performed the leakage current density measurements to test the SiO_2 dielectric layer by sweeping the gate bias from -8 to 8V.

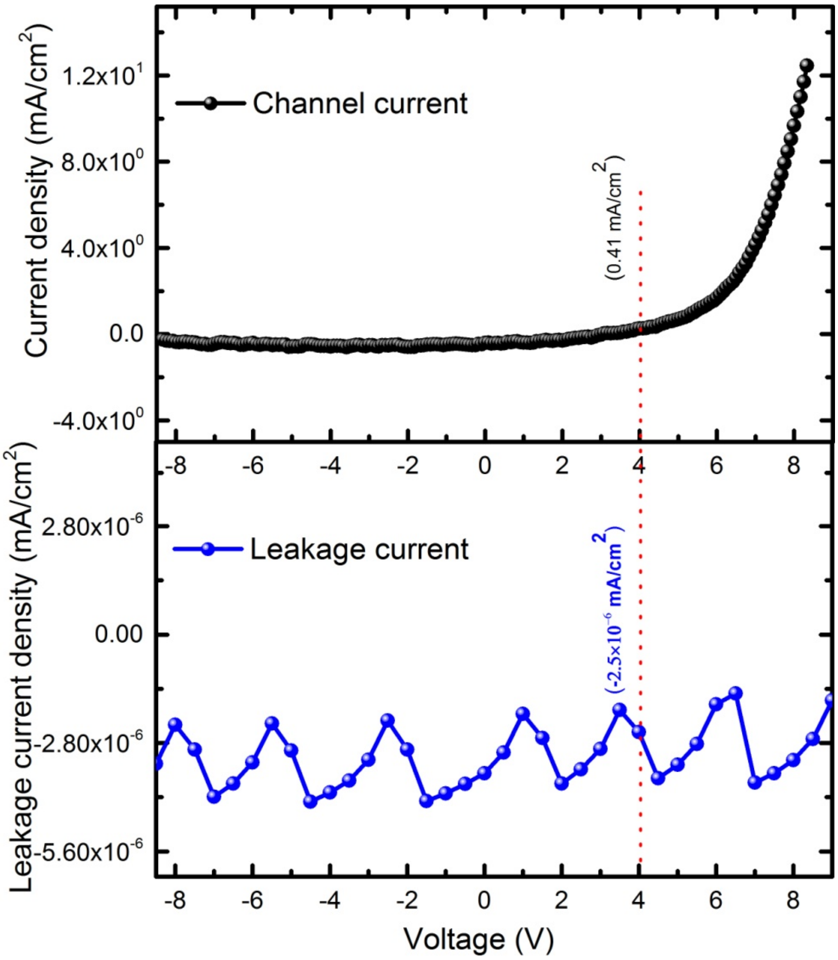

Fig. S4. A leakage current density test on the 20 nm-thick SiO_2 dielectric layer was conducted by scanning the gate bias from -8 to 8 V for four cycles. A typical plot of the leakage current density as a function of gate voltage is shown in the lower panel. A comparison of the channel current density (in the upper panel) with the leakage current density (in the lower panel) is presented with the values of current density being labeled at the gate bias of 4 V.

S5. Calculations for luminous efficiency and luminous efficacy

Both luminous efficiency (η) and luminous efficacy (μ) are important factors to evaluate LED performance. While the luminous efficiency (η) is defined as the ratio of luminous flux to electric power consumption, the luminous efficacy (μ) is defined as the ratio of luminous flux to optical power. The luminous efficiency (η) and luminous efficacy (μ) at each bias are calculated as,

For 2 V,

$$\eta\ (at\ 2V) = \frac{\phi v}{Electrical\ Power} = \frac{Km \int_{380}^{780} \phi e[\lambda]\ V[\lambda] d\lambda}{IV} = \frac{0.1702}{2 \times 0.37} = 0.23\ lm/W \times 100 = 23\%$$

$$\mu\ (at\ 2V) = \frac{\phi v}{Optical\ Power} = \frac{Km \int_{380}^{780} \phi e[\lambda]\ V[\lambda] d\lambda}{\int_{380}^{780} \phi e[\lambda]} = \frac{0.1702}{1.04 \times 10^{-3}} = 163\ lm/W$$

For 4V,

$$\eta\ (at\ 4V) = \frac{\phi v}{Electrical\ Power} = \frac{Km \int_{380}^{780} \phi e[\lambda]\ V[\lambda] d\lambda}{IV} = \frac{0.3097}{4 \times 0.26} = 0.29\ lm/W \times 100 = 29\%$$

$$\mu\ (at\ 4V) = \frac{\phi v}{Optical\ Power} = \frac{Km \int_{380}^{780} \phi e[\lambda]\ V[\lambda] d\lambda}{\int_{380}^{780} \phi e[\lambda]} = \frac{0.3097}{1.05 \times 10^{-3}} = 294\ lm/W$$

For 6V,

$$\eta\ (at\ 6V) = \frac{\phi v}{Electrical\ Power} = \frac{Km \int_{380}^{780} \phi e[\lambda]\ V[\lambda] d\lambda}{IV} = \frac{0.1092}{6 \times 1.82} = 0.01\ lm/W \times 100 = 1\%$$

$$\mu\ (at\ 6V) = \frac{\phi v}{Optical\ Power} = \frac{Km \int_{380}^{780} \phi e[\lambda]\ V[\lambda] d\lambda}{\int_{380}^{780} \phi e[\lambda]} = \frac{0.1092}{9.99 \times 10^{-4}} = 109\ lm/W$$

For 8V,

$$\eta\ (at\ 8\ V) = \frac{\phi v}{Electrical\ Power} = \frac{Km \int_{380}^{780} \phi e[\lambda]\ V[\lambda] d\lambda}{IV} = \frac{0.0824}{8 \times 9.68} = 0.001\ lm/W \times 100 = 0.1\%$$

$$\mu\ (at\ 8V) = \frac{\phi v}{Optical\ Power} = \frac{Km \int_{380}^{780} \phi e[\lambda]\ V[\lambda] d\lambda}{\int_{380}^{780} \phi e[\lambda]} = \frac{0.0824}{9.80 \times 10^{-4}} = 84\ lm/W$$

Table S2. A comparison of the obtained device's luminescence efficiency with a typical GaN LED.

Material/Structure	Luminescence Efficiency (lm/W)	Light Emission Color	Reference
p-MoS2/n-MoS_2/GaN	29	White	This work
GaN	11.5	Blue	J. Mater. Chem. C, 4 (2016) 2457

REFRENCES

[S1] P. Y. Yu and M. Cardona, *Fundamentals of Semiconductors-Physics and MaterialsProperties,* Springer-Verlag, Berlin Heidelberg, **2001.**

[S2] C.-W. Chang, W.-C.Tan, M.-L.Lu, T.-C.Pan, Y.-J.Yang, Y.-F. Chen, *Adv.Funct.Mater.*, 23 (2013) 4043–4048.